Laser Interference Lithography for the Nanofabrication of Stimuli-Responsive Bragg Stacks

*Nan Jiang, Haider Butt, Yunuen Montelongo, Feng Liu, Samson Afewerki, Guo-Liang Ying, Qing Dai, Seok-Hyun Yun, and Ali K. Yetisen**

Dynamic structural coloration in *Tmesisternus isabellae* beetle elytra is a unique example of Bragg stack-based wavelength tuning in response to external stimuli. The underlying principles could guide the design of quantitative optical stimuli-responsive polymers. Existing nanofabrication techniques to create such materials are costly, time-consuming, and require high expertise. This study reports a nanofabrication method to produce slanted Bragg stack structures in poly(acrylamide-*co*-poly(ethylene glycol) diacrylate) hydrogel films by combining laser interference lithography and silver halide chemistry in a cost-effective and rapid process (≈10 min). The Bragg stacks consist of silver bromide nanocrystal multilayers having a lattice spacing of ≈200 nm. Upon broadband light illumination, the Bragg stacks diffract a narrow-band peak at 520 nm at ≈10° with respect to the normal incidence. The lattice spacing of the hydrogel films can be modulated by external stimuli to shift the Bragg peak for dynamic quantitative measurements. To demonstrate the utility of this method, the Bragg stacks are functionalized with phenylboronic acid molecules. Bragg peak shift analysis allows reversible glucose sensing within a physiological dynamic range (0.0–20.0 mmol L^{-1}) having a sensitivity of 0.2 mmol L^{-1}. The developed Bragg stacks may have application in portable, wearable, and implantable real-time medical diagnostics at point-of-care settings.

1. Introduction

Since Robert Hooke and Isaac Newton's early observations of structural color in peacock tail feathers and mother of pearl in the 17–18th centuries, electron microscopy investigations have revealed the existence of diverse nanophotonic structures in nature from 1D to 3D photonic crystals.[1] Dynamic structural coloration is rare in nature and its evolutionary functions include Batesian mimicry, camouflage, conspecific recognition, predation, signal communication, and mating behavior.[2] It involves the diffraction of an incoming broadband light (sunlight) from a hierarchy of nanostructures, in which the periodicity can be modulated within the spectrum, ranging from ultraviolet light to near-infrared region.[2a] For example, the reflective stripes of the paradise whiptail (*Pentapodus paradiseus*) contain physiologically active iridophores.[3] Using the periodically stacked structure in its stripe, it can tune the color of the stripe from

Dr. N. Jiang, Dr. S. Afewerki, Dr. G.-L. Ying
Biomaterials Innovation Research Center
Engineering in Medicine Division
Brigham and Women's Hospital
Harvard Medical School
Cambridge, MA 02139, USA

Dr. N. Jiang, Dr. S. Afewerki, Dr. G.-L. Ying, Prof. S.-H. Yun, Dr. A. K. Yetisen
Harvard-MIT Division of Health Sciences and Technology
Massachusetts Institute of Technology
Cambridge, MA 02139, USA
E-mail: akyetisen@gmail.com

Dr. N. Jiang
State Key Laboratory of Advanced Technology for Materials Synthesis and Processing
Wuhan University of Technology
122 Luoshi Road, Wuhan 430070, China

Dr. H. Butt
Nanotechnology Laboratory
School of Engineering
University of Birmingham
Birmingham B15 2TT, UK

Dr. Y. Montelongo
Department of Chemistry
Imperial College London
London SW7 2AZ, UK

Dr. Y. Montelongo
Universidad De La Salle Bajío
León 37150, Mexico

Prof. F. Liu
Department of Physics
Shanghai Normal University
Shanghai 200234, China

Dr. G.-L. Ying
School of Materials Science and Engineering
Wuhan Institute of Technology
Wuhan 430205, China

Prof. Q. Dai
National Center for Nanoscience and Technology
Beijing 100190, China

Prof. S.-H. Yun, Dr. A. K. Yetisen
Harvard Medical School and Wellman Center for Photomedicine
Massachusetts General Hospital
65 Landsdowne Street, Cambridge, MA 02139, USA

ultraviolet to blue to achieve interspecies recognition and communication. The Hercules beetle (*Dynastes Hercules L*) contains a yellow sponge layer with periodic pillars, which display black color.[4] The color of the beetle can reversibly change from black to greenish yellow in a reversible manner when subjected to changes in humidity for thermoregulation and camouflage. The golden tortoise beetle (*Charidotella sexpunctata*) shows color changes in its cuticle from yellow to red by switching its chirped multilayer reflector to a translucent slab exposing pigmentary red substrate underneath to mimic unpalatable ladybird.[2b] Chameleons (*Furcifer pardalis*) adapt to their surroundings by displaying rapid structural color changes through active modulation of guanine NC spacing in dermal iridophores for camouflage purposes.[5]

A simple arrangement to create dynamic coloration in nature is through anatomic modulation of 1D photonic crystals (Bragg stacks), where a multilayer grating produces light interference under broadband illumination.[6] A striking example of dynamic structural coloration with Bragg stacks is observed in *Tmesisternus isabellae* (longhorn beetles), which exhibits color changes in its elytra in response to humidity.[7] The function of this evolutionary adaptation is unknown. **Figure 1** shows color changes of the beetle elytra in response to low (40%), interim (60%) to high (80%) relative humidity. The elytra showed bright golden-yellow iridescent color under broadband light in 40% relative humidity, while the color changed from orange-red to red when the relative humidity was increased to 80% (Figure 1a). Optical microscopy investigations of the

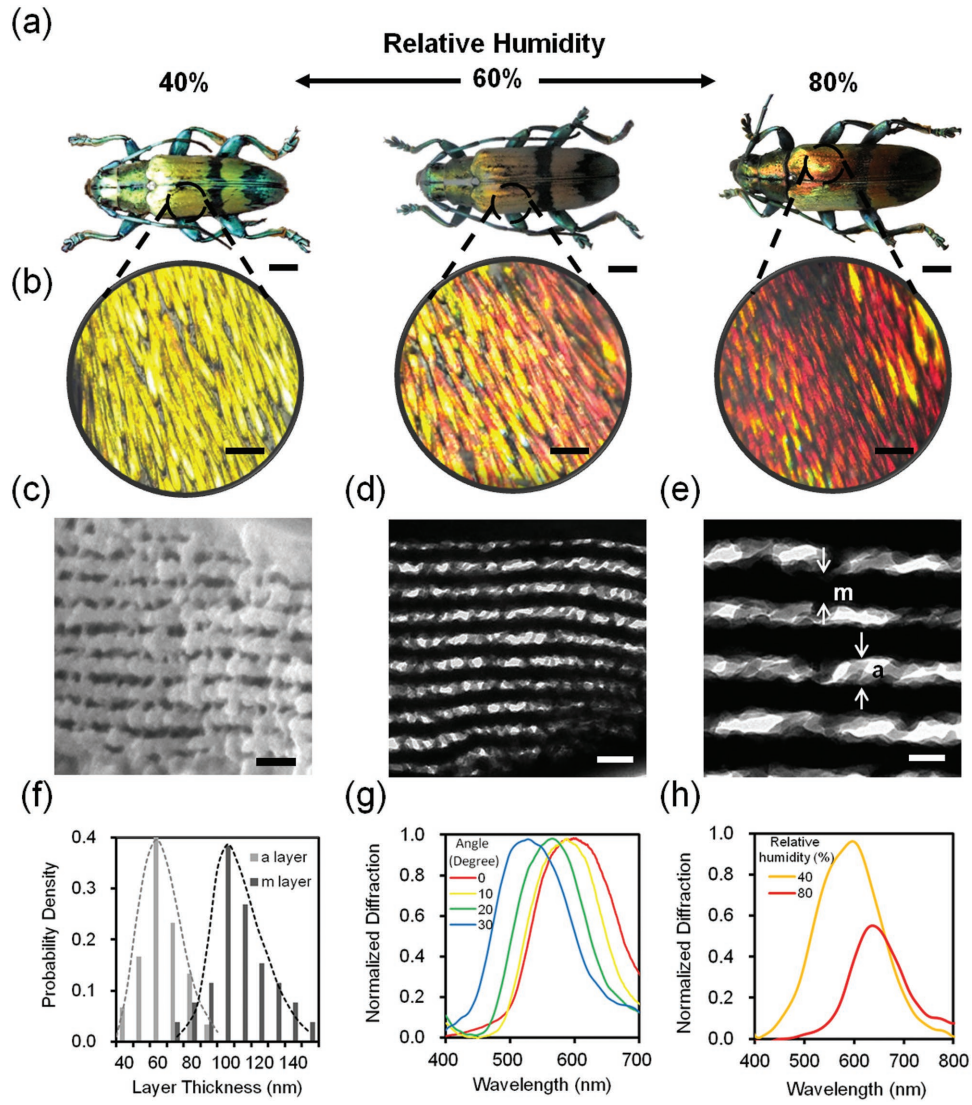

Figure 1. Structural color changes of the *Tmesisternus isabellae* elytra stimulated by humidity. a) Photographs of color changes of beetle elytra in low (40%), interim (60%), high (80%) relative humidities. Scale bar = 2.0 mm. b) Optical microscopy images of color changes of the elytra under broadband light in different humidity conditions. Scale bar = 50 µm. c) Transverse cross-section SEM image of the beetle elytra. Scale bar = 500 nm. d) Transverse cross-section TEM image of the elytra showing a Bragg stack structure. Scale bar = 400 nm. e) Magnified TEM image of the Bragg stack structure. The "m" and "a" layers represent the melanoprotein layer and the air gap layer, respectively. Scale bar = 200 nm. f) Melanoprotein and air layer thickness distributions in the beetle elytra. g) Angle-resolved measurements of the beetle elytra. h) Normalized diffraction spectra of the elytra in low (40%) and high (80%) relative humidity conditions.

beetle elytra showed that the dynamic coloration originated from the long scales on the elytra surface at different relative humidity conditions (40–60%) (Figure 1b; Movie S1, Supporting Information). Specifically, the structural coloration of the beetle elytra was synthesized from the multilayer interference in Bragg stacks, which could be tuned by physiological or external stimuli.[8] Figure 1c–e and Figure S1 in the Supporting Information show the scanning electron microscopy (SEM) and transmission electron microscopy (TEM) images of the multilayer structure of elytra. The elytra were composed of alternating layers of melanoprotein (110 ± 20 nm in thickness) consisting of densely packed nanoparticles and air gaps (65 ± 15 nm) (Figure 1f; Figure S2, Supporting Information). The beetle elytra were bleached by hydrogen peroxide to reveal the presence of melanin (Figure S3, Supporting Information).[9] Angle-resolved measurements also revealed that the Bragg peak shifted from 600 to 530 nm as the diffraction collection angle was increased from 0° to 30° with respect to normal incidence (Figure 1g). When the relative humidity (40%) was increased to 80%, water infiltration and subsequent swelling of the multilayers shifted (33 nm) the diffracted peak to longer wavelengths (Figure 1h). The decrease in the diffraction efficiency by ≈44% was owing to the decreased effective refractive index (RI) of the multilayers.[7a] Water absorption by the melanoprotein layer swelled the multilayer structure and shifted the diffraction peak (λ_{max}), obeying Bragg-Snell's law (Equation (1))[6,10]

$$\lambda_{max} = 2(n_m d_m \cos\theta_m + n_a d_a \cos\theta_a) \quad (1)$$

where n_m (≈2.0) and n_a (≈1.2) represent the RIs of melanoprotein layer and air gap layer, d_m and d_a are the thicknesses of melanoprotein layer and the air gap layer, and θ_m and θ_a are the refraction angles with respect to normal incidence. The maximum theoretical diffraction efficiency that can be obtained from the beetle elytra was calculated to be 75% in the visible spectrum.[11] This high diffraction efficiency can be attributed to both high RI of the melanoprotein layers and the low RI of the air gap layers, providing ideal conditions for light interference and diffraction. However, the infiltration of water into the elytra fills the air gaps and swells the melanoprotein layer. As a consequence, water infiltration decreases the RI of the Bragg stack, decreasing the diffraction efficiency by more than 40%. Additionally, the hierarchical distribution of the elytra over the dorsal side of the beetle ensures that the diffraction can be observed from large viewing angles. The beetle elytra have shown the ability to sense humidity changes by diffracted color changes. Hence, these physical principles of dynamic structural coloration can be used as a guideline to create tunable optical nanostructures to quantitatively sense analyte changes.[12]

Based on the understanding of the exquisite hierarchical dynamic structures in nature, several bottom-up and top-down nanofabrication approaches have been developed to create stimuli-responsive nanophotonic structures.[13] Bottom-up nanofabrication approaches include layer-by-layer deposition, self-assembly of diblock copolymers, and spin coating.[11a,14] These approaches have challenges due to time-consuming layer deposition, inability to functionalize layers, and uneven layer thicknesses, as well as high-cost laborious production of Bragg stacks.[15] As a top-down nanofabrication approach, LIL has emerged as a rapid and flexible technique to produce multilayer gratings.[16] LIL is a maskless technique that creates Bragg stacks by using two or more coherent laser waves.[17] The commonly used pulsed laser (nanosecond or femtosecond) provides a high peak power that allows the formation of Bragg stacks by laser ablation.[18] In addition to the high cost of nanosecond pulsed laser ($1–50 k),[18a,19] the laser ablation-based production of Bragg stacks is affected by nanoparticle light scattering, particle attenuation, and damage to the recording medium, limiting the diffraction efficiency of the resulting photonic nanostructure. The multiphoton absorption polymerization can also be utilized to fabricate Bragg stacks; however, they are limited as active radicals that polymerize monomers in the antinodes diffuse into the dark fringe regions, which results in relatively low resolution.[20]

Continuous wave (CW) laser light interference combined with silver halide chemistry provides a cost-effective method to create controllable Bragg stacks with high diffraction efficiency. However, the fabrication of Bragg stacks by CW laser interference typically requires complex laser optics and setups.[21] The need for high-cost pulsed or CW laser setups and optical equipment complexity have limited the adoption of LIL in photonic nanostructure production.[22] Additionally, due to the complexity of optical laser writing setups involving the alignment of multiple mirrors and beam expanders, the systems require stabilization to reduce environmental vibrations. Hence, there is a clear need to develop a cost-effective nanofabrication method that allows Bragg stacks to be fabricated rapidly and reproducibly Bragg stacks without the need for complex laser optics.

In this work, we created a cost-effective LIL nanofabrication method for rapid production of Bragg stacks embedded in hydrogel films. A low-cost portable laser diode was utilized to create a periodic interference pattern within the photosensitized *p*(AM-*co*-PEGDA) hydrogel film in Denisyuk reflection mode. A latent image was recorded using silver halide chemistry to form periodic AgBr NC multilayers in the hydrogel film. To demonstrate the utility of the stimuli-responsive Bragg stacks, the *p*(AM-*co*-PEGDA) hydrogel backbone was functionalized with 3-(acrylamido)phenylboronic acid (3-APBA) to produce a reversible response to variation in glucose concentration, which was correlated with Bragg peak shifts to obtain quantitative measurements.

2. Results and Discussion

To rationally design a Bragg stack that can dynamically operate in the visible spectrum, a finite element method was utilized to model and study a multilayer structure. In a dynamically tunable system, it is expected that as the lattice spacing increases, the Bragg peak will shift to longer wavelengths (**Figure 2**a). To build the Bragg stacks, AgBr NCs were chosen due to its light-sensitivity and high RI (2.28, $\lambda = 546$ nm). The designed domain was modeled to simulate a polymer film (thickness ≈ 10 μm, RI ≈ 1.46) with alternating multilayer AgBr NC stacks. These Bragg stacks filter incoming broadband light and diffract narrow-band rays in the visible spectrum. Figure 2b shows the finite element simulations of Bragg stacks having lattice spacings ranging from 150 to 180 nm. The wave propagation

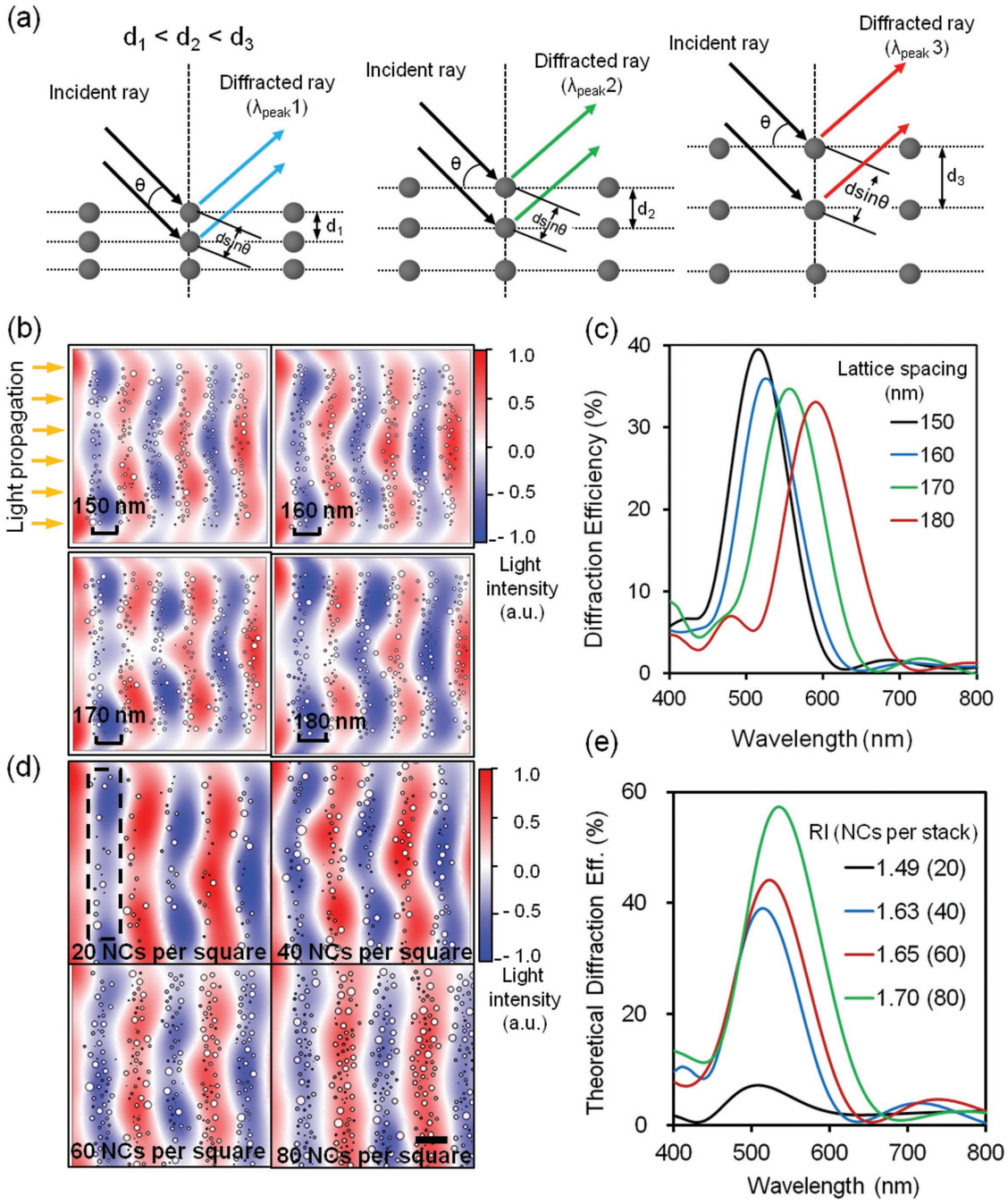

Figure 2. Finite-element simulations of tunable Bragg stacks. a) Expansion of lattice spacing in a Bragg stack shifts the diffracted ray to longer wavelengths. b) Simulated geometries and wave propagation results for the Bragg diffracted waves of the multilayered structures. c) The simulated diffraction spectra for different lattice spacings. d) Simulated geometries and wave propagation results for different effective RIs (AgBr NC density) of the Bragg stacks. Scale bar = 150 nm. Dashed areas show counted nanoparticles per stack. e) The simulated diffraction spectra for different effective RI values within the Bragg stacks.

simulations for a lattice spacing of 150 nm showed a Bragg peak position of 520 nm. This wavelength defines the green-diffracted color of the Bragg stacks, where the Bragg peak position is primarily dictated by the lattice spacing between the AgBr NC stacks. The effect of lattice spacing expansion on the position and intensity of the Bragg peak was also analyzed. As the number of the Bragg stacks and AgBr NCs were kept constant (40 NCs per stack), the Bragg stack geometry was laterally expanded. The lateral expansion increased the lattice spacing of the Bragg stacks and reduced the concentration of AgBr NCs within a stack. As the lattice spacing increased from 150 to 180 nm, the diffracted spectra produced a red-shift, changing the color from green to orange (Figure 2c). The diffraction efficiency of the Bragg stack peak decreased by 15%, while the

lattice spacing increased by 30 nm. This phenomenon could be ascribed to the decreased concentration of AgBr NCs within a stack reducing the RI contrast between the stacks and the surrounding medium. According to the Bragg's law, the diffraction spectrum could be correlated to the effective RI of the stacks and their lattice spacing. The factors that influence the diffraction ray could be described as (Equation (2))[11a]

$$\frac{\Delta\lambda}{\lambda} = \frac{\Delta n}{n} + \frac{\Delta d}{d} + \cot\theta\ \Delta\theta \tag{2}$$

where $\Delta\lambda$, Δn, Δd, $\Delta\theta$ are changes in Bragg peak wavelength, effective RI, lattice spacing, and diffraction angle. To analyze the outcome of effective RI changes (Δn) within the Bragg stacks, the concentration of AgBr NCs was varied within a Bragg stack, where d (150 nm) and θ (90° from the normal incidence) were kept constant (Figure 2d). As the effective RI of the AgBr NC stack was increased from 1.49 to 1.70 (corresponding to 20 to 80 AgBr NCs per stack), the diffraction efficiency increased by 83% (Figure 2e). This indicated that increasing AgBr NCs density enhanced the diffraction efficiency. Additionally, the increase in the effective RI of the stack by 0.21 resulted in the Bragg peak shift by ≈30 nm to longer wavelengths.

The Bragg stack embedded in a 10 µm thick *p*(AM-*co*-PEGDA) hydrogel film was fabricated by free-radical polymerization on a silanized glass surface (Table S1 and Scheme S1, Supporting Information). The Bragg stacks within the hydrogel matrix were formed by a cost-effective and rapid LIL method involving silver halide chemistry (**Figure 3**a; Table S2, Supporting Information). Ag^+ ions were diffused into the synthesized hydrogel film (Figure 3a-i). Photosensitization was achieved by exposing the hydrogel film to a solution containing LiBr and acridine orange dye, which converted the Ag^+ ions to photosensitive AgBr NCs (Figure 3a-ii,b-i). An optical interference setup was configured to operate in Denisyuk reflection mode for writing a latent image within the hydrogel matrix using a CW laser diode (λ = 532 nm, 5 mW) (Figure 3a-iii,b-ii).[23] Ascorbate buffer was diffused into the hydrogel film, which was sandwiched using another glass substrate. The photosensitive film was placed on a leveled surface tilted (5°) from the surface plane of a plane mirror. Figure 3c shows the optical setup for writing a latent image in the AgBr NCs using the portable laser diode. The inset in Figure 3c shows the mechanism of the laser light interference of an incident beam (reference wave) and a reflected beam from the plane mirror (object wave). The constructive interference (antinodes) corresponded to high laser intensity regions of a standing wave. This process created a multilayer latent image within the hydrogel film.

Upon the formation of an interference pattern, photosensitive dye on the surface of AgBr NCs absorbed photons. The process underwent proton-coupled electron transfer, in which electrons transferred from a ground state to an excited state, subsequently releasing electrons ($AgBr + h\nu \rightarrow Ag^+ + Br^0 + e^-$) (Figure 3d).[24] The interstitial Ag^+ ion left its original position to an "interlattice" space due to thermal equilibrium (Figure 3e-i; Equation S1, Supporting Information). The released electrons migrated to an electron trap zone in the latent image site, offering a negatively charged trap zone (Figure 3e-ii). The intensity of the laser exposure light determined the amount of photon–electron transfer in the photosensitive dye. However, the ascorbate buffer (pH 6.0) also acted as the electron source for photo-induced electron transfer (Scheme S2, Supporting Information). In electron conduction stage, the negatively charged site attracted positively charged interstitial Ag^+ ions that were deposited in the latent image site (Figure 3e-iii). When the interstitial Ag^+ ions reached to the trap site, the positive charge was neutralized ($Ag^+ + e^- \rightarrow Ag^0$). The Ag speck was formed by accumulating Ag atoms on the latent image site (Figure 3e-iv). The latent image was amplified using a photographic developer. The reduction of AgBr NCs to Ag^0 NPs is normally carried out using a highly alkaline developer (pH > 12).[25] However, alkaline developers distort the polymer chains and results in hydrolyzation.[26] In the present work, a neutral developer was used to convert Ag atoms in the AgBr NCs to Ag^0 NPs (Figure 3a-iv). The neutral developer provided electrons that allowed Ag^+ ions in the "interlattice" position to adhere to the latent image Ag atoms (Scheme S3, Supporting Information). Therefore, the Ag^0 NPs grew until the developer was neutralized by decreasing the pH using acetic acid (Figure 3a-v). The excess AgBr grains and conjugated photosensitive dye were removed from the hydrogel matrix by rinsing with a hypo solution containing sodium thiosulfate (Figure 3a-vi,b-iii). The unreacted Ag^+ ions and AgBr NCs are binded to the terminal sulfur in thiosulfate to form soluble compounds (Scheme S4, Supporting Information).

Ag^0 NPs can be used as diffractive layers in Bragg stacks; however, the RI of Ag^0 NPs ($n = 0.14 + i\ 3.14$, λ = 546 nm) results in low diffraction efficiency.[27] Low diffraction efficiency makes the diffracted peak of Bragg stacks difficult to be observed or detected, which affects the performance of the sensor including sensitivity, response and reset time, and detection limits. To increase the diffraction efficiency of the Bragg stacks, Ag^0 NPs were converted back to AgBr NCs by copper sulfate oxidation in a bleaching bath containing Br^- ions (Figure 3a-vii; Scheme S5, Supporting Information). The reduced Cu^0 NPs in the hydrogel film were removed by an antiprintout solution containing persulfate and hydrogen sulfate ions (Figure 3a-viii,b-iv; Scheme S6, Supporting Information). Meanwhile, free bromide produced from the solution attached to the AgBr NCs surface and acted as a strong oxidant to protect the AgBr NCs from converting back to Ag^0 NPs by photolysis. Movie S2 in the Supporting Information shows a simulation of the entire LIL process to produce the Bragg stacks. The whole fabrication process was performed in less than 10 min.

The process of latent image formation in LIL has been studied to understand the optical properties of the Bragg stacks. To simulate LIL patterning process, the exposure radiant fluence and fabrication speed were defined as ≈50 mJ cm^{-2} and 0.5 $cm^2\ s^{-1}$, respectively. The fabricated hydrogel film was measured to be ≈10 µm thick (Figure S4, Supporting Information). **Figure 4**a shows the field distribution within a 10 µm thick recording medium with a tilt angle of 5°, where the absorption was assumed to be 18%. The incidence laser beam (λ = 532 nm) was propagated through the boundary in Denisyuk reflection mode. The localization of light intensity had an essential role in the standing wave formation. The decrease in the exposure radiant fluence was 18% over a ≈10 µm propagation distance (Figure 4b). The localized standing wave intensity had a lattice spacing of ≈200 nm (Figure 4b inset; Figure S5,

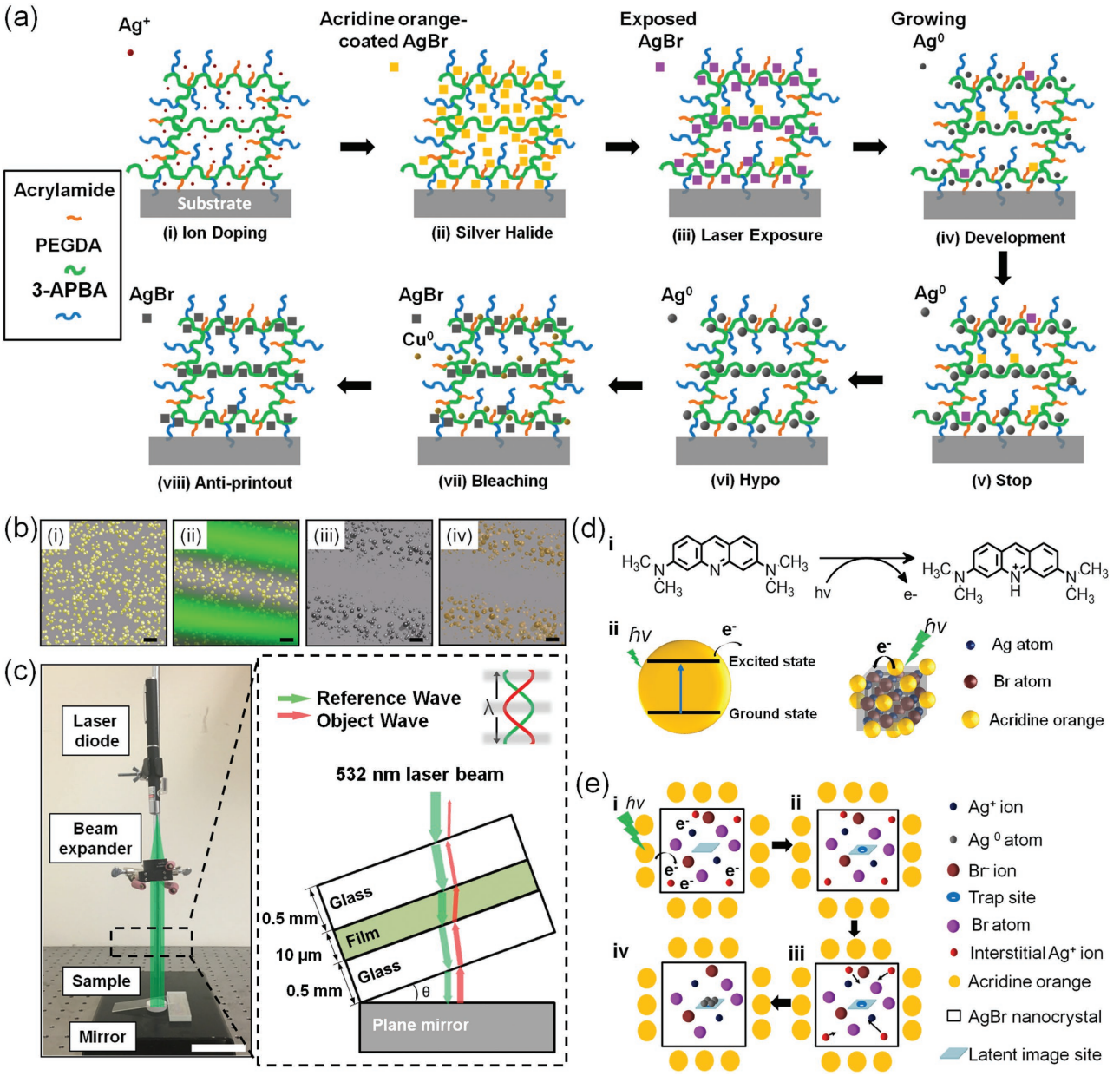

Figure 3. Fabrication of a Bragg stack using LIL in hydrogel films. a) Formation of a latent image and grating in silver halide chemistry. (i) Ag^+ ions ($AgNO_3$, 100 mmol L^{-1}) were diffused into the hydrogel film, (ii) AgBr NC formation, (iii) latent image formation, (iv) the reduction of AgBr NCs to Ag^0 NPs using a neutral developer, (v) stop bath, (vi) hypo to remove undeveloped AgBr NCs, (vii) bleaching solution to convert Ag^0 NPs to AgBr NCs, and (viii) antiprintout bath to etch Cu^0 NPs. b) Simulation of AgBr NC growth within the light inference domain in Denisyuk reflection mode. (i) Formation of photosensitive AgBr NCs distributed within the hydrogel film; (ii) creation of the latent image under the laser exposure; (iii) formation of multilayers consisting of Ag^0 NP stack; (iv) Bragg stacks having multilayer AgBr NCs. Scale bar = 30 nm, c) Denisyuk reflection mode was setup to record a latent image using a CW laser diode (λ = 532 nm, 5.0 mW). Scale bar = 5.0 cm. The inset shows standing wave formation. d) Energy transfer between acridine orange and AgBr NCs. e) Latent image formation in AgBr NCs: (i) absorption of a photon and electron transfer from acridine orange to the AgBr NCs, (ii) formation of a negatively charged electron trap zone, (iii) the migration of interstitial Ag^+ ions to the trap zone, and (iv) the reduction of Ag^+ ions to Ag^0 atoms and formation of a Ag speck (latent image).

Supporting Information). Along with the vertical periodicity to form a multilayer exposure pattern, a lateral interference pattern having a periodicity of ≈1.5 µm was also observed and this could be attributed to the internal reflections.

The diffraction spectra of Bragg stacks were collected using a spectrophotometer with the illumination of incident broadband light (Figure S6, Supporting Information). The Bragg stacks containing AgBr NCs diffracted green color with diffraction efficiency of 9% (Figure 4c,d). Moreover, the Bragg stacks in the form of hydrogel films were shaped to various geometries such as free-standing round flakes (Ø = 2.0 mm). The hydrogel flakes maintained green diffraction color under broadband

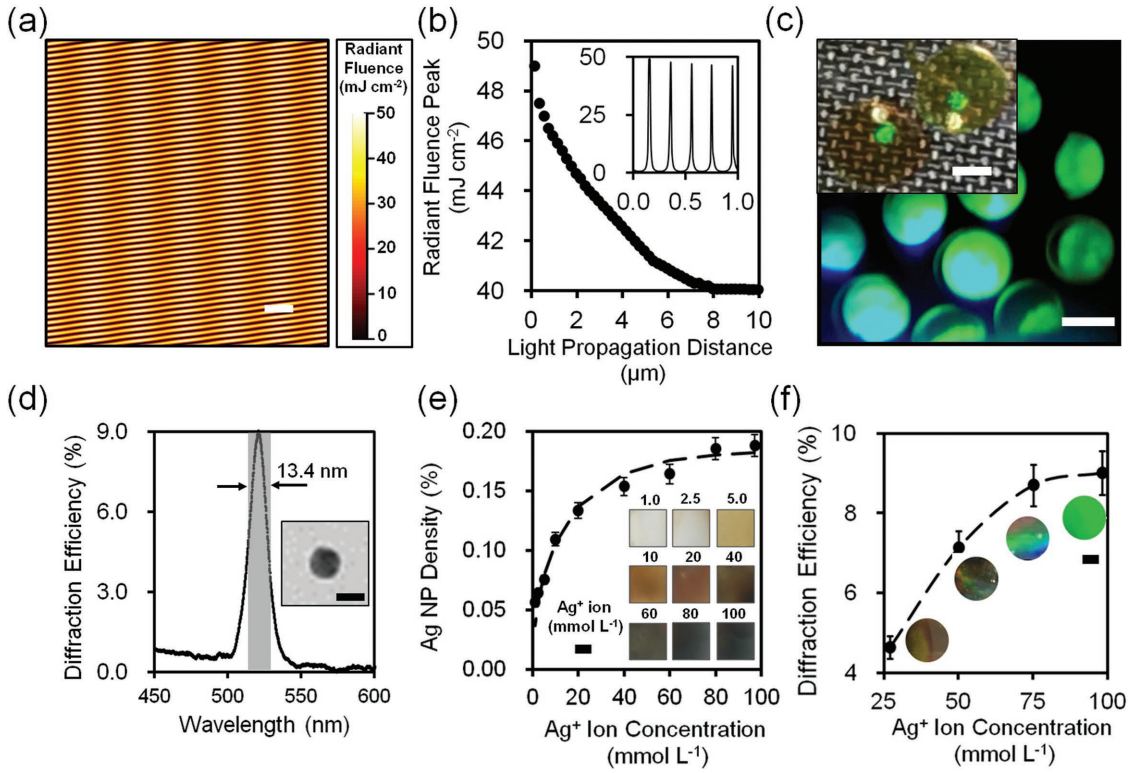

Figure 4. Characterization of the *p*(AM-*co*-PEGDA) Bragg stack films. a) The field distribution generated by light interference within the hydrogel film with a tilt angle of 5°, created by two waves: reference wave and object wave. Scale bar = 1.0 µm. b) Laser light interference propagation within the whole hydrogel matrix with a propagation distance of 10 µm. Peaks represent standing wave peak. Inset shows light interference propagation with a propagation distance of 1 µm. c) A photograph of Bragg stacks produced by silver halide chemistry. Scale bar = 200 µm. Inset shows a photograph of two substrate-free Bragg stack flakes. Scale bar = 1 mm. d) Diffraction spectrum. Inset shows a TEM image of an embedded single Ag^0 NP within hydrogel film. Scale bar = 10 nm. e) Ag^0 NPs density within hydrogel matrix. Insets show the photographs of hydrogel films loaded with different concentrations of Ag^0 NPs ($n = 3$). Scale bar = 2.0 mm. f) The effect of Ag^+ ion concentration on diffraction efficiency of the Bragg stacks consisting of AgBr NCs ($n = 3$). Inset shows the photographs of hydrogel films. Scale bar = 2.0 mm. Error bars represent standard deviation.

light (Figure 4c inset). The spectrum of the Bragg stacks containing AgBr NCs had a central peak at ≈520 nm and diffracted light at ≈10° from the normal interference and the full width at half-maximum was 13.4 nm (Figure 4d). The fabricated Ag^0 NP Bragg stack was shown in Figure S4b in the Supporting Information and the size of the Ag^0 NPs was ≈10 nm (Figure 4d inset). To understand the parameters that affect the diffraction efficiency, the Ag^+ ion concentrations in the hydrogel films were analyzed. As the Ag^+ ion concentration in the hydrogel film increased from 1.0 to 100.0 mmol L^{-1}, the density of the formed Ag^0 NPs increased from 0.08% to 0.20% and it saturated at a Ag^+ ion concentration of ≈80 mmol L^{-1} (Figure 4e). The diffraction efficiency of the AgBr NC stack increased from 4.2% to 8.5% as the Ag^+ ion concentration increased from 25 to 100 mmol L^{-1} (Figure 4f). The diffraction efficiency of Bragg stack was saturated at Ag^+ ion concentration of 100 mmol L^{-1}, which was consistent with the saturation point of Ag^0 NPs density within the hydrogel film.

To demonstrate the utility of the Bragg stacks, a phenylboronic acid derivative was incorporated to render the hydrogel matrix sensitive to glucose.[28] Phenylboronic acid derivatives have been known to covalently bind with *cis*-diol groups of carbohydrates to form boronic esters.[29] Figure S7 in the Supporting Information shows the reversible complexation equilibrium of phenylboronic acid with *cis*-diol groups of glucose molecules.[30] At low pH value, the phenylboronic acid is in trigonal planar form (unchanged state), which does not complex with glucose. However, above its p*Ka* value (> 8.8), the phenylboronic acid is in tetrahedral state (negatively charged state), which can readily bind with *cis*-diol groups of glucose.[31] When the phenylboronic acids are incorporated within a hydrogel matrix, they can be used as reversible and real-time glucose-responsive hydrogel films. In the presence of a high ionic strength buffer (150 mmol L^{-1}), the hydrogel was fully swollen prior to experiments. Hence, the complexion of phenylboronic acid and the *cis*-diol groups of glucose molecules in subsequent hydrogel expansion could be explained by the modified Flory–Huggins theory (Equations S2–S6, Supporting Information).[32,33] *p*(AM-*co*-PEGDA-*co*-3-APBA) hydrogel flakes responding to glucose were investigated and *p*(AM-*co*-PEGDA) hydrogel flakes were used as a control. The optimization in PEGDA and 3-APBA showed that the precursor of the hydrogel with AM (77 mol%), PEDGA (3 mol%), and 3-APBA (20 mol%) had the largest expansion (2.9%) in response to glucose (10 mmol L^{-1}, 24 °C) which was optimal for glucose response. The complexation of 3-APBA and glucose reached to the saturation points after 40 min. When glucose molecules diffused into the *p*(AM-*co*-PEGDA-*co*-3-APBA) hydrogel films,

glucose–boronic acid complexation decreased the pK_a of the PBA groups upon *cis*-diol binding, resulting in charged boronate groups. The formation of anionic boronate increased the Donnan osmotic pressure of the system, resulting in hydrogel swelling. The hydrogel expansion curves were fitted to Equation (3), which describes the hydrogel diameter expansion ($\Delta\varnothing(t)$) correlated with glucose diffusion dynamics

$$\Delta\varnothing(t) = \Delta\varnothing_{\infty}\sqrt{1 - e^{-\alpha t}} \quad (3)$$

where $\Delta\varnothing_{\infty}$ is the hydrogel flake diameter expansion after an infinite time, α represents the decay constant, and t is the diffusion time. When using higher concentrations of PEGDA as the crosslinker (4.0 and 3.5 mol%), the elasticity of the hydrogel flake decreased, resulting in the flake diameter expansions of 1.7% and 2.5%, respectively. However, the hydrogel flakes with low concentration of PEGDA (2.5 and 2.0 mol%) did not show significant swelling (2.2% and 1.1% diameter expansion) (**Figure 5**a). With increasing 3-APBA concentration (25 and 30 mol%) at a constant PEGDA concentration (3 mol%), the hydrogel flake diameter expansion was limited to 1.7% and 1.1%, respectively. This could be attributed to the decreased in AM concentration. Another factor that affected hydrogel expansion was the low solubility of 3-APBA in deionized (DI) water. At low concentrations of 3-APBA (10 and 15 mol%), the hydrogel swelling was low (1.1 and 2.6 mol%) due to low complexion of phenylboronic acid and *cis*-diol groups of glucose molecules (Figure 5b). The effect of the pH value on hydrogel flakes expansion depended on the apparent pK_a value. Hydrogel flakes expanded 5.9% by increasing the pH value of the buffer solution (150 mmol L^{-1}) from 4.5 to 9.0 (Figure 5c; Figure S8 and Table S3, Supporting Information). Apparent p*K*a value of the hydrogel flake was calculated from the modified Henderson–Hasselbalch equation, which could be expressed as (Equation (4))

$$\varnothing_{shift} = \Delta\varnothing\left(1 + 10^{(pKa - pH)}\right)^{-1} \quad (4)$$

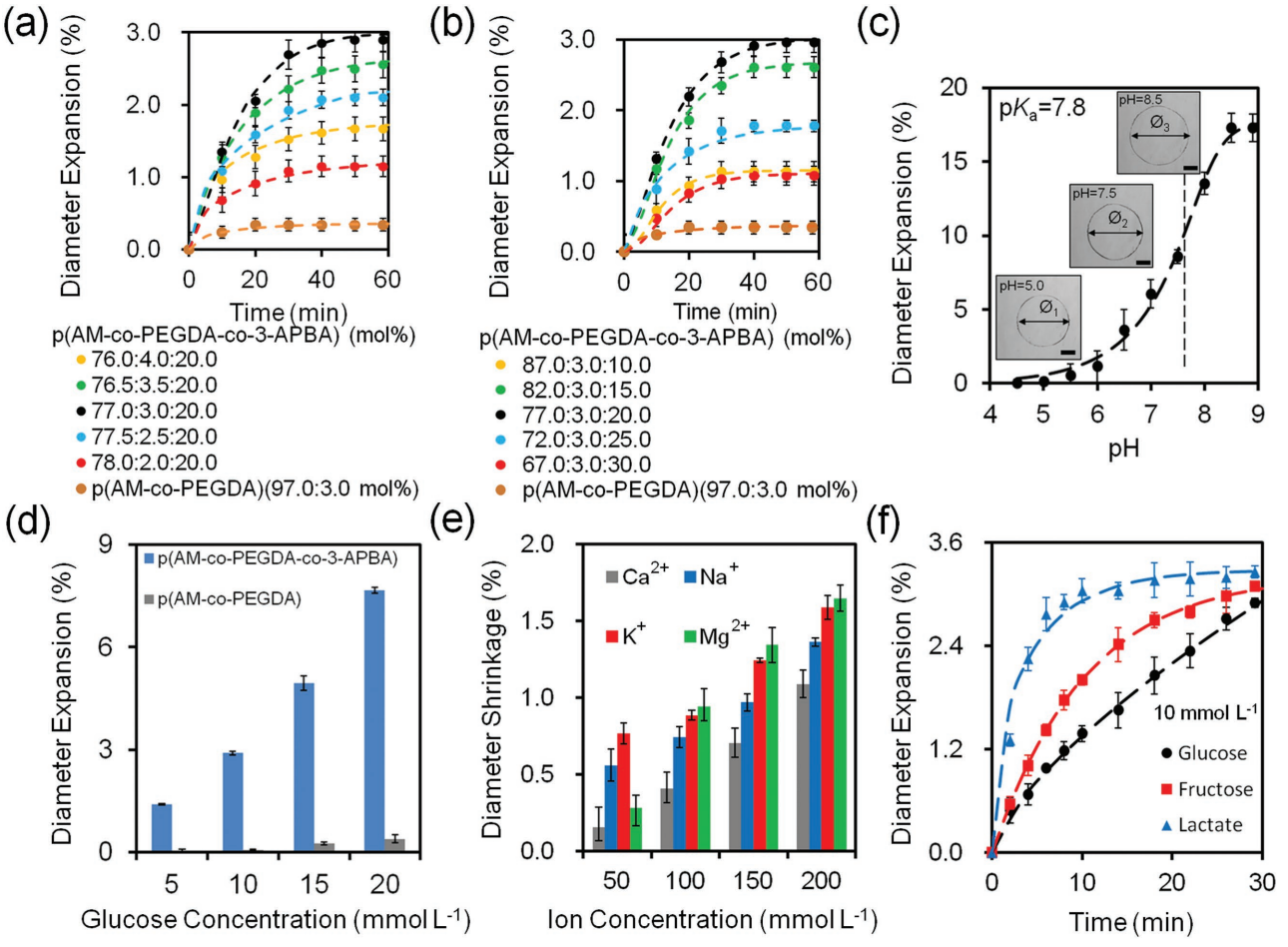

Figure 5. Quantification of glucose concentration with *p*(AM-*co*-PEGDA-*co*-3-APBA) film at pH 7.4 at 24 °C. The hydrogels were fully swollen during the measurements. a) Time-lapse measurements of the expansion of hydrogel flake diameter (Ø = 2 mm) by varying concentrations of PEGDA in the presence of glucose (10 mmol L^{-1}) and control experiments fitted with the exponential decay equation, where the decay constant α was 1.9×10^{-2} s^{-1} ($n = 3$). b) Time-lapse measurements of the expansion of hydrogel flake diameter (Ø = 2 mm) by varying concentrations of 3-APBA in the presence of glucose (10 mmol L^{-1}) and control experiments fitted with the exponential decay equation ($n = 3$). c) pH-dependent hydrogel flake expansion (10 mmol L^{-1}) ($n = 3$). $\varnothing_1$, $\varnothing_2$, and $\varnothing_3$ represent diameters at pH value of 5.0, 7.5, and 8.5, respectively. Scale bar = 1.0 mm, the curve is fit to Equation (4). d) The change in the diameter of the hydrogel flakes as the glucose concentration increasing from 5 to 20 mmol L^{-1} ($n = 3$). e) Ionic effect on hydrogel flake shrinkage ($n = 3$). f) Hydrogel flake response to glucose, fructose, and lactate (10 mmol L^{-1}) ($n = 3$). Error bars represent standard deviation.

where $Ø_{shift}$ is the hydrogel flake diameter change, ΔØ represents the difference between maximum and minimum of flake diameter, p*K*a represents the acid dissociation constant. Based on Equation (4), the apparent p*K*a value was ≈7.8. As the glucose concentration increased within the physiological range from 5 to 20 mmol L^{-1}, the *p*(AM-*co*-PEGDA-*co*-3-APBA) hydrogel flake diameter expansion increased from 1.4% to 7.7% within 40 min. Without 3-APBA molecules, hydrogel flakes did not show significant expansion (Figure 5d; Figure S9 and Table S4, Supporting Information). The effect of ionic strength on hydrogel shrinkage was also investigated by immersing hydrogel flakes in metal ion solutions (Na^+, K^+, Ca^{2+}, and Mg^{2+} ions, pH = 7.4). As ion concentrations increased from 50 to 200 mmol L^{-1}, the diameter of hydrogel flakes shrunk 0.8%, 0.8%, 0.9%, and 1.4%, respectively (Figure 5e; Figure S10 and Table S5, Supporting Information). The fully swollen hydrogel flake shrinkage could be attributed to the increase in counterions that amplified the Donnan osmotic pressure.[34] The interference in hydrogel expansion might be caused by physiological fructose and lactate commonly found analytes in biological samples, which could also bind to 3-APBA. Due the its smaller molecular weight (Mw = 90 g mol^{-1}), lactate rapidly diffused into the hydrogel matrix and bound to boronic acid groups, achieving fast equilibrium within 20 min. Replacing the glucose solution with fructose solution (pH = 7.4) resulted in a higher hydrogel flake expansion (3.1%) within 30 min as compared to glucose (2.7%) (Figure 5f; Figure S11 and Table S6, Supporting Information). These results were consistent with the previous studies that showed that boronic acid had higher affinity to fructose than glucose.[35]

After the optimization of the phenylboronic acid formulation, a Bragg stack was incorporated into a hydrogel film to create an analytical device to quantitatively report the concentration of glucose. The phenylboronic acid-*cis*-diol complexation and subsequent hydrogel swelling increased the lattice spacing of periodically distributed AgBr NC stacks, shifting the Bragg peak to longer wavelengths (**Figure 6**a). The concentration of glucose can be correlated with the wavelength of the Bragg peak. In the presence of a glucose solution (100 mmol L^{-1}) in buffer (pH 7.4, 150 mmol L^{-1}) at 24 °C, the peak of Bragg

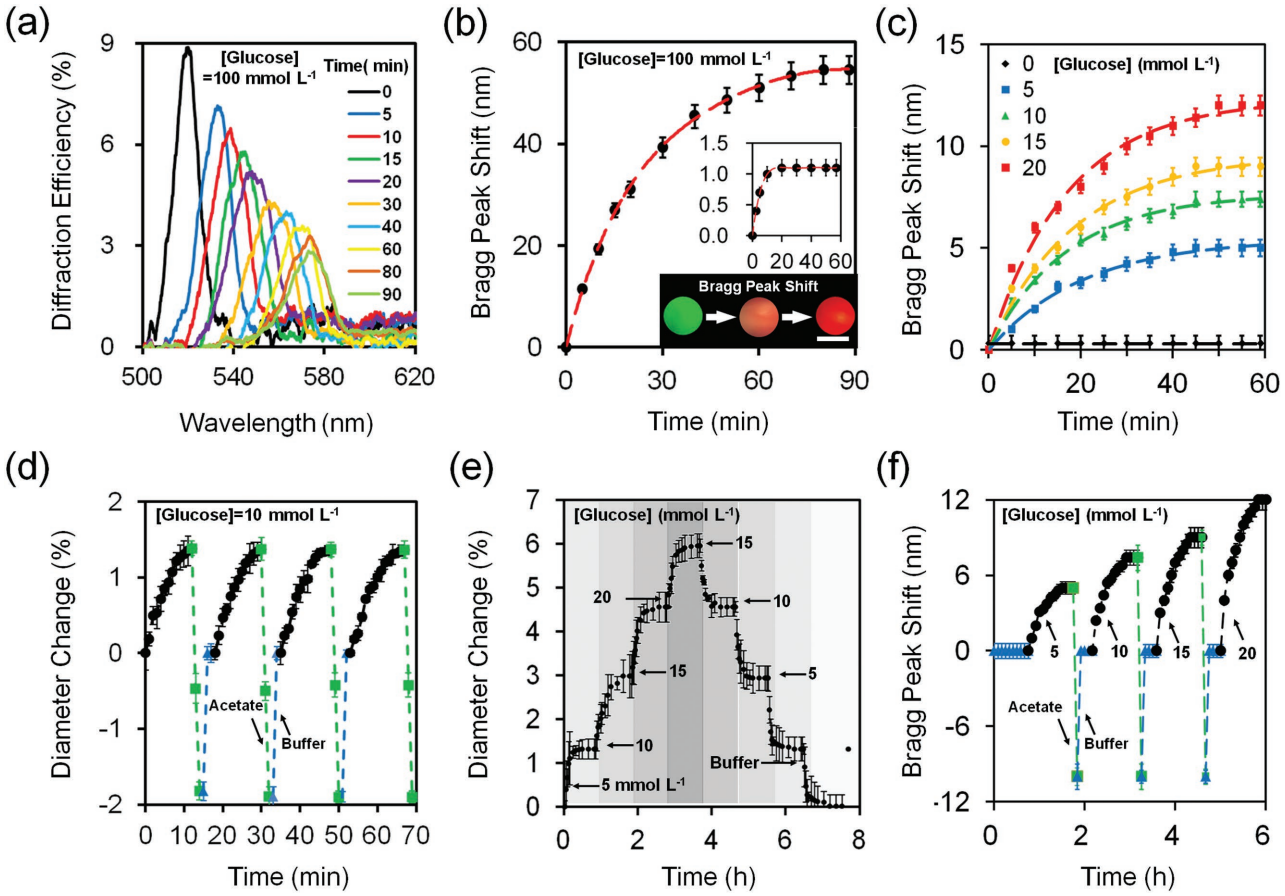

Figure 6. Quantifications of glucose concentrations and reversibility. a) Diffraction spectra of a Bragg stack hydrogel film in response to glucose (100 mmol L^{-1}) over 90 min. The dashed line was fitted using Equation (7), where the constants were c = 99 nm, λ_0 = 452 nm, and I_0 = –0.45. b) The peak shift of the Bragg stacks as a function of time (n = 3). Insets show colorimetric readouts of the Bragg stacks, and the control experiment without 3-APBA (n = 3). Scale bar = 2.0 mm. c) Quantification of glucose by the Bragg stacks within the physiological glucose range (n = 3). The dashed lines were fitted using Equation (7). d) Reset experiment of the hydrogel flakes by varying glucose solution (10 mmol L^{-1}) and acetate buffer (pH = 4.6) (n = 3). The hydrogel flake diameter was returned to its original size by using acetate buffer, followed by buffer rinse. e) Reversibility of the hydrogel film in glucose sensing (n = 3). Arrows show applied glucose concentrations. f) Reusability of the Bragg stacks responding to glucose in continuous measurements based on diffracted peak shifts (n = 3). Arrows show applied glucose concentrations. Error bars represent standard deviation.

stack shifted from its original position at 520 to 576 nm in 90 min (Figure 6b). Bragg stacks synthesized without 3-APBA comonomers shifted the diffraction peak by 1–2 nm, indicating its crucial role in glucose complexation (Figure 6b inset). The minimum resolution of the Bragg peak that could be measured using a spectrophotometry was 0.50 nm, which correlated to a minimal lattice spacing swelling of 0.17 nm. Theoretically, the Bragg stack hydrogel film (≈10 μm in thickness) needs to swell to a minimum of 8.8 nm to produce a resolvable wavelength shift in the spectrum.

The diffraction efficiency of the Bragg stacks asymptotically decreased by ≈65% during the hydrogel film expansion, which could be owing to the decreased concentration of the AgBr NCs per stack. The correlation between the maximum diffraction intensity and the position of the Bragg peak was (Equation (5))

$$DE_{max} \approx DE_0 + \frac{c}{\lambda_{peak} - \lambda_0} \tag{5}$$

where DE_0 and λ_0 are the asymptotes of the fitting curve, and c is a constant. As the Bragg peak shifted 50 nm (from 520 to 570 nm), the diffraction efficiency decreased 5.4%, which was consistent with the simulated 5.5% decrease of diffraction efficiency as the Bragg peak shifted from 510 to 560 nm (Figure 2c). The Bragg peak shift was associated with visible color changes from green to orange to orange-red (Figure 6b inset). The complexation of the anionic boronate with *cis*-diol groups of glucose molecules showed an exponential decay over time. The characteristics of the Bragg stacks response were modeled by analyzing the dynamic Bragg peak shift behavior in response to glucose. During complexation, the concentration of the bound glucose molecules can be expressed as (Equation (6))

$$C_i(t) = C_\infty(1 - e^{-\gamma t}) \tag{6}$$

where C_∞ is the amount of anionic boronate form at infinite time, γ is the binding rate of boronic acid-*cis*-diol complexation, and t is the analyte complexation time. Within the physiological range of glucose concentration, the complexation is proportional to the Bragg peak shift

$$\Delta\lambda(t) = \Delta\lambda_\infty(1 - e^{-\gamma t}) \tag{7}$$

where $\Delta\lambda_\infty$ represents the equilibrated Bragg peak shift. Therefore, Equation (7) can be used to describe Bragg peak shift over time. The response of the Bragg stack to glucose concentration was tested within physiological glucose conditions (e.g., diabetic range of 3–20 mmol L^{-1}, normal: 4.2–6.4 mmol L^{-1}) (Figure 6c; Figure S12, Supporting Information). The Bragg stack was fully swollen before the measurements. With boronate anion and glucose complexation, the Donnan osmotic pressure increased and the Bragg peak shifted by 5 and 12 nm for glucose concentrations of 5 and 20 mmol L^{-1}, respectively, over 1 h. The Bragg peak shift saturated with increasing glucose concentrations (Equation (7)). The average sensitivity of the Bragg stack was calculated to be 0.2 mmol L^{-1} (Figure S13 "Sensitivity of the Bragg Stacks", Supporting Information).

The reversibility of the glucose-responsive Bragg stack was measured. Four consecutive hydrogel resetting experiments were performed within 70 min in a buffered glucose solution (10 mmol L^{-1}) (Figure 6d). Replacing the glucose solution with an acetate buffer (pH = 4.6) resulted in hydrogel shrinkage. This process broke the covalent bonds between the phenylboronic acids and *cis*-diols of glucose. The hydrogel swelled back to its original size by replacing the acetate buffer with a glucose-free phosphate buffered saline (PBS) solution (pH = 7.4), enabling reusability of the glucose-responsive hydrogel. As the glucose-free solution was replaced with a glucose solution (20 mmol L^{-1}), the diameter of the hydrogel flake expanded by 4.6%. When the glucose solution was replaced with a glucose-free solution, the hydrogel shrank by 3.4% (Figure 6e).

Subsequent experiments were performed to validate the hydrogel reversibility with a Bragg stack. When the glucose-free solution was replaced with a glucose solution (5 mmol L^{-1}), the Bragg peak shifted by 5 nm over 1 h at 24 °C (Figure 6f). The replacement of the glucose solution (pH 7.4) with acetate buffer (pH 4.6) transformed the tetrahedral state of anionic boronate to an uncharged trigonal state, releasing the glucose molecules from the hydrogel matrix within 10 s. The decrease in the lattice spacing of the Bragg stack with acetate buffer could be attributed to the decrease of pH below the apparent pK_a value of the hydrogel, shifting the Bragg peak to shorter wavelengths (λ_{peak} = 510 nm). When the acetate buffer was replaced with a glucose-free buffer solution (pH 7.4), the Bragg peak shifted to its original position (λ_{peak} = 520 nm) and no hysteresis was measured in resetting the Bragg stack over multiple trials (Figure 6f). As glucose-free solutions were replaced with glucose solutions at concentrations of 10, 15, and 20 mmol L^{-1}, the Bragg peak shifted 7.4, 8.9, and 12.0 nm, respectively, which was consistent with the results of individual measurements of each glucose concentration (Figure 6c). The Bragg peak shifted to shorter wavelengths (λ_{peak} = 510 nm) when acetate buffer was applied for resetting. These results demonstrated that the phenylboronic acid functionalized Bragg stack could be used for the reversible glucose measurements without hysteresis.

3. Conclusion and Discussion

Dynamic structural colorations of *T. isabellae* elytra in response to the variations in environmental humidity were attributed to Bragg peak shifts from the alternating melanoprotein-air layers. To reproduce this multilayer structure and resemble its dynamic coloration properties, we created a cost-effective method to rapidly fabricate a stimuli-responsive slanted Bragg stack by combining LIL and silver halide chemistry. The produced Bragg stack could accurately report the changes of glucose concentrations by diffraction peak shifts without being affected by intensity changes. However, as compared to high diffraction efficiency in beetle elytra (≈75%), the fabricated Bragg stack had low diffraction efficiency (≈9%) due to the low effective RI contrast and low particle density within the hydrogel film. To improve the diffraction efficiency, the AgBr NCs density can be improved by utilizing more hydrophilic polymers for optimal $AgNO_3$ perfusion into the hydrogel matrix. The AgBr NCs can also be replaced by high-RI materials such as TiO_2 nanoparticles and synthetic photopolymers which can tune the RI by varying concentrations of polymer.[36] The melanoproteins could

be used to produce Bragg stacks by a layer-by-layer deposition process.[37] However, the melanoproteins as pigments, they are easily affected from bleaching, which could render Bragg stack sensors instable. Furthermore, the Bragg stack had a narrow diffraction angle (≈10°), which required a specialized spectroscopy setup to measure the diffraction peak shifts. To overcome this challenge, angular tolerance can be improved by replacing the plane mirror with a convex mirror during the LIL process to distribute the diffracted light broader angles (Figure S14, Supporting Information).[11a] Moreover, the object used to create the latent image can be substituted with other complex structures to form a wide range of grating shapes (e.g., arrays, 2/3D patterns and images).[18a]

To improve the selectivity for glucose, other PBA derivatives can be utilized, such as 2-(acrylamido)phenylboronate, *bis*-boronic acid, and 4-vinylphenylboronic acid.[31,38] Additionally, the hydrogel matrix can be functionalized with other receptors to create selectivity for other analytes including ions, proteins, and microorganisms.[15a,22,39] The sensitivity of the Bragg stack hydrogel can also be enhanced by using other highly elastic polymers which could increase the polymer swelling in response to external stimuli. Synthesizing the hydrogel matrix to produce nanoporous structures and a gating membrane can enhance analyte diffusion and complexation rate by increasing the surface area.[40] The Bragg stack hydrogels can be easily shaped to various geometries such as flakes that can be integrated with commercial test strips or implantable devices.[28,41] A single hydrogel film on a microscopy glass slide can be shaped to at least 200 flakes, which has a cost of ≈$0.15 per device. The demonstrated cost-effective LIL patterning method has the potential to rapidly produce Bragg stacks at mass scale using a laser diode setup. These Bragg stacks may find a wide range of applications in disease diagnostics, toxicity detection, and drug discovery.

4. Experimental Section

Characterization of Beetle Elytra: Beetle elytra were treated by serial dehydration using ethanol and propylene oxide, and embedded within Epoxy. Ultrathin cross-sections of samples were utilized for SEM and TEM imaging. The diffraction spectra were measured using microspectrum analysis equipment with an aperture normal incidence at ≈3°.

Modeling and Fabrication of Bragg Stacks: The AgBr NC stacks within hydrogel were simulated using a finite-element method. The Bragg stack sensor was fabricated by LIL combined with silver halide chemistry. Briefly, a monomer solution containing AM (77 mol%), PEGDA (3 mol%), 3-APBA (20 mol%), and 2-HMP in DI water (2%, v/v) was pipetted on a silanized glass slide. The *p*(AM-*co*-PEGDA-*co*-3-APBA) hydrogel film was formed by UV exposure for 3 min. The unreacted monomers were removed from the hydrogel matrix by rinsing with ethanol and DI water.[28] The Bragg stacks fabrication process was performed over eight steps. (1) $AgNO_3$ solution was diffused into the hydrogel film and dried under a tepid air current; (2) The hydrogel film was treated with LiBr-acridine orange solution (photosensitization solution) for 40 s and rinsed with DI water. (3) The photosensitized hydrogel film was immersed in an ascorbate buffer and sandwiched with another clean glass slide. The sandwiched hydrogel film was placed on a leveled plane mirror and tilted 5° from the surface plane in Denisyuk reflection mode. (4) The hydrogel film was exposed to the laser light (λ = 532 nm, 5 mW) for 10 s under red safe lighting to form a latent image of a multilayer stack. (5) The hydrogel film was immersed in a neutral photographic developer consisting of 2,4-diaminophenol dihydrochloride (75 mmol L^{-1}), sodium sulfite (125 mmol L^{-1}), and sodium carbonate (65 mmol L^{-1}) for 1 min. (6) The hydrogel film was submerged in a stop bath containing acetic acid (2 vol%) for 1 min to stop the action of the developer. (7) The unexposed AgBr NCs within the film were removed by a hypo solution containing sodium thiosulfate (0.6 mol L^{-1}) for 10 min. (8) The Bragg stacks were submerged in an antiprintout solution containing sodium persulfate (0.8 mol L^{-1}) and sodium hydrogen sulfate (0.3 mol L^{-1}) for 3 min.

Glucose Sensing by Bragg Peak Shift Measurement: Glucose (100 mmol L^{-1}) and glucose-free solutions in PBS (pH 7.4) were mixed to prepare concentrations ranging from 5 to 20 mmol L^{-1}. Bragg stack hydrogel film was placed in a cuvette containing glucose solutions. The measurement was performed using a spectrophotometer under broadband light. The diffraction spectra from the spectrophotometer were recorded at 5 min time intervals.

Supporting Information

Supporting Information is available from the Wiley Online Library or from the author.

Acknowledgements

The authors acknowledge Ali Khademhosseini, Guillermo U. Ruiz-Esparza, Amir Sheikhi, Amir Nasajpour, Roberto Parra Saldivar, Wei Geng, and Tongxiang Fan for discussion. H.B. thanks Wellcome Trust and Leverhulme Trust for the research funding. G.L.Y. thanks Hubei Provincial Natural Science Foundation of China (No. 2014CFB778).

Conflict of Interest

The authors declare no conflict of interest.

Keywords

Bragg stacks, laser interference lithography, optical sensors, phenylboronic acids, silver halide chemistry

[1] P. Vukusic, J. R. Sambles, *Nature* **2003**, *424*, 852.
[2] a) J. Sun, B. Bhushan, J. Tong, *RSC Adv.* **2013**, *3*, 14862; b) J. P. Vigneron, J. M. Pasteels, D. M. Windsor, Z. Vértesy, M. Rassart, T. Seldrum, J. Dumont, O. Deparis, V. Lousse, L. P. Biró, *Phys. Rev. E* **2007**, *76*, 031907; c) D. Stuart-Fox, A. Moussalli, *Philos. Trans. R. Soc., B* **2009**, *364*, 463.
[3] L. Mäthger, M. Land, U. Siebeck, N. Marshall, *J. Exp. Biol.* **2003**, *206*, 3607.
[4] a) H. Hinton, G. Jarman, *Nature* **1972**, *238*, 160; b) H. Hinton, G. Jarman, *J. Insect Physiol.* **1973**, *19*, 533541.
[5] J. Teyssier, S. V. Saenko, D. Van Der Marel, M. C. Milinkovitch, *Nat. Commun.* **2015**, *6*, 6368.
[6] T. Lu, W. Peng, S. Zhu, D. Zhang, *Nanotechnology* **2016**, *27*, 122001.
[7] a) F. Liu, B. Dong, X. Liu, Y. Zheng, J. Zi, *Opt. Express* **2009**, *17*, 16183; b) H.-b. Seo, S.-Y. Lee, *Sci. Rep.* **2017**, *7*, 44927.

[8] S. Kinoshita, S. Yoshioka, J. Miyazaki, *Rep. Prog. Phys.* **2008**, *71*, 076401.
[9] J. Whittaker, *Biochim. Biophys. Acta* **1979**, *583*, 378.
[10] Y. Yue, T. Kurokawa, M. A. Haque, T. Nakajima, T. Nonoyama, X. Li, I. Kajiwara, J. P. Gong, *Nat. Commun.* **2014**, *5*, 4659.
[11] a) A. K. Yetisen, I. Naydenova, F. da Cruz Vasconcellos, J. Blyth, C. R. Lowe, *Chem. Rev.* **2014**, *114*, 10654; b) K. Nonaka, *Appl. Opt.* **1997**, *36*, 4792.
[12] a) K. Sano, Y. S. Kim, Y. Ishida, Y. Ebina, T. Sasaki, T. Hikima, T. Aida, *Nat. Commun.* **2016**, *7*, 12559; b) L. Phan, R. Kautz, E. M. Leung, K. L. Naughton, Y. Van Dyke, A. A. Gorodetsky, *Chem. Mater.* **2016**, *28*, 6804.
[13] M. Xiao, Y. Li, J. Zhao, Z. Wang, M. Gao, N. C. Gianneschi, A. Dhinojwala, M. D. Shawkey, *Chem. Mater.* **2016**, *28*, 5516.
[14] a) C. Zhang, G. G. Cano, P. V. Braun, *Adv. Mater.* **2014**, *26*, 5678; b) Y. Y. Diao, X. Y. Liu, G. W. Toh, L. Shi, J. Zi, *Adv. Funct. Mater.* **2013**, *23*, 5373; c) M. Chen, L. Zhou, Y. Guan, Y. Zhang, *Angew. Chem., Int. Ed.* **2013**, *52*, 9961; d) Y. Kang, J. J. Walish, T. Gorishnyy, E. L. Thomas, *Nat. Mater.* **2007**, *6*, 957.
[15] a) Z. Cai, D. H. Kwak, D. Punihaole, Z. Hong, S. S. Velankar, X. Liu, S. A. Asher, *Angew. Chem. Int. Ed.* **2015**, *54*, 13036; b) Z. Cai, L. A. Luck, D. Punihaole, J. D. Madura, S. A. Asher, *Chem. Sci.* **2016**, *7*, 4557.
[16] a) M. Deubel, G. Von Freymann, M. Wegener, S. Pereira, K. Busch, C. M. Soukoulis, *Nat. Mater.* **2004**, *3*, 444; b) A. Selimis, V. Mironov, M. Farsari, *Microelectron. Eng.* **2015**, *132*, 83; c) J.-H. Seo, J. H. Park, S.-I. Kim, B. J. Park, Z. Ma, J. Choi, B.-K. Ju, *J. Nanosci. Nanotechnol.* **2014**, *14*, 1521.
[17] S. Zhu, Y. Fu, J. Hou, *Lithography: Principles, Processes and Materials*, Nova Science Publishers, Hauppauge, NY, USA **2011**.
[18] a) Y. Montelongo, A. K. Yetisen, H. Butt, S.-H. Yun, *Nat. Commun.* **2016**, *7*, 12002; b) A. K. Yetisen, Y. Montelongo, F. da Cruz Vasconcellos, J. Martinez-Hurtado, S. Neupane, H. Butt, M. M. Qasim, J. Blyth, K. Burling, J. B. Carmody, *Nano Lett.* **2014**, *14*, 3587.
[19] Thorlabs, NPL52B –Nanosecond Pulsed Laser Diode System, 520 nm, 5 –39 ns Adjustable Pulse Width, https://www.thorlabs.com/ (accessed: August 2017).
[20] L. Li, J. T. Fourkas, *Mater. Today* **2007**, *10*, 30.
[21] W.-C. Su, K.-T. Kuo, presented at *Microopt. Conf. (MOC), 20th*, Fukuoka, Japan, Oct., **2015**.
[22] A. K. Yetisen, Y. Montelongo, M. M. Qasim, H. Butt, T. D. Wilkinson, M. J. Monteiro, S. H. Yun, *Anal. Chem.* **2015**, *87*, 5101.
[23] S. A. Benton, V. M. Bove, *Holographic Imaging*, Wiley-Interscience, Hoboken, NJ **2007**, p. 173.
[24] R. Gurney, N. Mott, *Proc. R. Soc. A* **1938**, *164*, 151.
[25] C. P. Tsangarides, A. K. Yetisen, F. da Cruz Vasconcellos, Y. Montelongo, M. M. Qasim, T. D. Wilkinson, C. R. Lowe, H. Butt, *RSC Adv.* **2014**, *4*, 10454.
[26] E. V. Tan, C. R. Lowe, *Anal. Chem.* **2009**, *81*, 7579.
[27] A. K. Yetisen, H. Butt, F. da Cruz Vasconcellos, Y. Montelongo, C. A. Davidson, J. Blyth, L. Chan, J. B. Carmody, S. Vignolini, U. Steiner, *Adv. Opt. Mater.* **2014**, *2*, 250.
[28] A. K. Yetisen, N. Jiang, A. Fallahi, Y. Montelongo, G. U. Ruiz-Esparza, A. Tamayol, Y. S. Zhang, I. Mahmood, S. A. Yang, K. S. Kim, H. Butt, A. Khademhosseini, S.-H. Yun, *Adv. Mater.* **2017**, *29*, 1606380.
[29] D. Lee, M. S. Taylor, *J. Am. Chem. Soc.* **2011**, *133*, 3724.
[30] T. D. James, K. S. Sandanayake, R. Iguchi, S. Shinkai, *J. Am. Chem. Soc.* **1995**, *117*, 8982.
[31] Y. Guan, Y. Zhang, *Chem. Soc. Rev.* **2013**, *42*, 8106.
[32] V. L. Alexeev, A. C. Sharma, A. V. Goponenko, S. Das, I. K. Lednev, C. S. Wilcox, D. N. Finegold, S. A. Asher, *Anal. Chem.* **2003**, *75*, 2316.
[33] P. J. Flory, *Principles of Polymer Chemistry*, Cornell University Press, Ithaca, NY **1953**.
[34] H. Li, *Smart Hydrogel Modelling*, Springer Science & Business Media, Heidelberg, Germany **2010**.
[35] W. Zhai, X. Sun, T. D. James, J. S. Fossey, *Chem. - Asian J.* **2015**, *10*, 1836.
[36] a) W. K. Smothers, B. M. Monroe, A. M. Weber, D. E. Keys, *Pract. Hologr. IV* **1990**, *1212*, 20; b) S. Paul, I. Vartiainen, M. Roussey, T. Saastamoinen, J. Tervo, S. Honkanen, M. Kuittinen, *Opt. Express* **2016**, *24*, 26901.
[37] M. Bruening, D. Dotzauer, *Nat. Mater.* **2009**, *8*, 449.
[38] a) X. Yang, M. C. Lee, F. Sartain, X. Pan, C. R. Lowe, *Chem. - Eur. J.* **2006**, *12*, 8491; b) S. Kabilan, J. Blyth, M. Lee, A. Marshall, A. Hussain, X. P. Yang, C. Lowe, *J. Mol. Recognit.* **2004**, *17*, 162; c) W. Zhai, B. M. Chapin, A. Yoshizawa, H.-C. Wang, S. A. Hodge, T. D. James, E. V. Anslyn, J. S. Fossey, *Org. Chem. Front.* **2016**, *3*, 918; d) W. Zhai, L. Male, J. S. Fossey, *Chem. Commun.* **2017**, *53*, 2218; e) D. H.-C. Chou, M. J. Webber, B. C. Tang, A. B. Lin, L. S. Thapa, D. Deng, J. V. Truong, A. B. Cortinas, R. Langer, D. G. Anderson, *Proc. Natl. Acad. Sci. USA* **2015**, *112*, 2401.
[39] J.-T. Zhang, Z. Cai, D. H. Kwak, X. Liu, S. A. Asher, *Anal. Chem.* **2014**, *86*, 9036.
[40] a) Q. Zhang, B. Chen, L. Tao, M. Yan, L. Chen, Y. Wei, *RSC Adv.* **2014**, *4*, 32475; b) Z. Liu, W. Wang, R. Xie, X.-J. Ju, L.-Y. Chu, *Chem. Soc. Rev.* **2016**, *45*, 460; c) X. Hou, W. Guo, L. Jiang, *Chem. Soc. Rev.* **2011**, *40*, 2385.
[41] J. D. Newman, A. P. Turner, *Biosens. Bioelectron.* **2005**, *20*, 2435.